Journal of Geophysical Research: Oceans

Supporting Information for

On the relation between seismic source dynamics, tsunami generation and propagation, and numerical modelling complexity in subduction zones

A. Scala[1,2], S. Lorito[2], C. Escalante Sanchez[3], F. Romano[2], G. Festa[1,2], A. Abbate[2,4], H. B. Bayraktar[2], M. J. Castro[3], J. Macias[3], J. M. Gonzalez-Vida[3]

[1] Department of Physics "Ettore Pancini", University Federico II, Napoli, 80126, Italy.

[2] Istituto Nazionale di Geofisica e Vulcanologia, Rome, 00143, Italy

[3]EDANYA Group, University of Malaga, Malaga, 29080, Spain

[4]Department of Mathematics and Geosciences, University of Trieste, 34128, Italy

Contents of this file

Text S1 to S2
Figures S1 to S16
Tables S1 and S3

Additional Supporting Information (Files uploaded separately)

Captions for Tables S2
Captions for Movies S1 to S10

Introduction

Within the following Supporting Information we include:

- a more detailed description of the tsunami numerical modelling scheme along with the validation of the presented scheme against some standard benchmark test
- 16 Figures to support the results presented in the main text
- 3 Tables summarizing:
    - Sampled seismic source parameters
    - Seismic source parameters selected for each simulation (only caption, Table S2 in a separate file)
    - Seismic source parameterization for real events reported in Figure 8
- 10 captions for the movie included to Supporting Information as separate files. The movies represent the animated wave evolution of simulations whose snapshots are plotted in Figures 2 and 3 (in the main text) and S12, S14 and S15 (in Supporting Information).

Text S1 Tsunami numerical modelling

We briefly describe the numerical discretization of system in equations (3)-(5) in the main text assuming a constant split of the layers $l_\alpha = 1/L$. Here, we follow the procedure described in Escalante et al. (2019). The numerical scheme is based on a two-step projection-correction method, similar to the standard Chorin's projection method for Navier-Stokes equations (Chorin, 1968). That is a standard procedure when dealing with dispersive systems (see Ma et al., 2012; Kazolea & Delis, 2013; Ricchiuto & Filippini, 2014; Escalante et al., 2018, 2019 and references therein).
First, we shall solve the non-conservative hydrostatic underlying system in equation (3) given by the compact equation:

$$\partial_t \mathbf{U} + \partial_x \mathbf{F}(\mathbf{U}) + \mathbf{B}(\mathbf{U})\partial_x \mathbf{U} + \mathbf{G}(\mathbf{U})\partial_x \eta = 0 \qquad \text{(S1)}$$

where the following compact notation has been used:

$$\mathbf{U} = \begin{pmatrix} h \\ hu_1 \\ \vdots \\ hu_L \\ hw_1 \\ \vdots \\ hw_L \end{pmatrix}, \ \mathbf{F}(\mathbf{U}) = \begin{pmatrix} hu \\ u_1 hu_1 \\ \vdots \\ u_L hu_L \\ u_1 hw_1 \\ \vdots \\ u_L hu_L \end{pmatrix}, \ \mathbf{G}(\mathbf{U}) = \begin{pmatrix} 0 \\ gh \\ \vdots \\ gh \\ 0 \\ \vdots \\ 0 \end{pmatrix}, \qquad \text{(S2)}$$

and $\boldsymbol{B}$ is a matrix such $\boldsymbol{B}\partial_x U$ contains the non-conservative products related to the mass transfer across interfaces appearing at the momentum equations.
Then, in a second step, the non-hydrostatic terms from the right-hand side of equations (3) collected by the pressure vector.

$$\mathcal{T}(h,\partial_x h,z_b,\partial_x z_b,\mathbf{P},\partial_x\mathbf{P}) = -L\begin{pmatrix} 0 \\ \frac{1}{2}h_1\partial_x(p_{3/2}+p_{1/2}) - (p_{3/2}-p_{1/2})\partial_x z_1 \\ \vdots \\ \frac{1}{2}h_L\partial_x\left(0+p_{L-\frac{1}{2}}\right) - \left(0-p_{L-\frac{1}{2}}\right)\partial_x z_L \\ h_1(p_{3/2}-p_{1/2}) \\ \vdots \\ h_L\left(0-p_{L-\frac{1}{2}}\right) \end{pmatrix}, \quad \mathbf{P} = \begin{pmatrix} p_{1/2} \\ p_{3/2} \\ \vdots \\ p_{L-1/2} \end{pmatrix} \tag{S3}$$

as well as the divergence constraints at each layer given in equation (5) will be taken into account. Concerning the constraints, we will equivalently impose

$$\mathcal{B}_\alpha = 0, \text{ where } \mathcal{B}_1 = \mathcal{I}_1,\ \mathcal{B}_2 = \mathcal{I}_2 - \mathcal{I}_1,\ \ldots,\ \mathcal{B}_L = \mathcal{I}_L - \mathcal{I}_{L-1} \tag{S4}$$

so that the divergence impositions read as follows:

$$\mathcal{B}\left(\mathbf{U}^{(k)},\partial_x\mathbf{U}^{(k)},z_b,\partial_x z_b\right) =$$

$$\begin{pmatrix} -h_1\partial_x(h_1u_1) + 2\partial_x z_1 h_1u_1 - 2h_1w_1 + 2h_1\partial_t z_b \\ -h_2\partial_x(h_2u_2) - h_1\partial_x(h_1u_1) + 2h_2u_2\partial_x z_2 - 2h_1u_1\partial_x z_1 - 2h_2w_2 + 2h_1w_1 \\ \vdots \\ -h_L\partial_x(h_Lu_L) - h_{L-1}\partial_x(h_{L-1}u_{L-1}) + 2h_Lu_L\partial_x z_L - 2h_{L-1}u_{L-1}\partial_x z_{L-1} - 2h_Lw_L + 2h_{L-1}w_{L-1} \end{pmatrix}. \tag{S5}$$

System in eq. (S1) is discretized using a second-order finite volume PVM positive-preserving well-balanced path-conservative method (Castro Díaz & Fernández-Nieto, 2012). As usual, we consider a set of N finite volume cells $I_i = [x_{(i-1/2)}\ , x_{(i+1/2)}]$ with constant lengths Δx and define:

$$\mathbf{U}_i(t) = \frac{1}{\Delta x}\int_{I_i}\mathbf{U}\,(x,t)\,dx \tag{S6}$$

the cell average of the function $U(x,t)$ on cell I_i at time t. Concerning non-hydrostatic terms, we consider mid-points x_i of each cell I_i and denote the point values of the function P at time t by:

$$\mathbf{P}_i(t) = \begin{pmatrix} p_{1/2}(x_i,t) \\ p_{3/2}(x_i,t) \\ \vdots \\ p_{L-1/2}(x_i,t) \end{pmatrix}. \tag{S7}$$

Non-hydrostatic terms will be approximated by second-order compact finite differences. Let us detail the time stepping procedure followed. Assume given time steps Δt^n , and denote $t^n = \sum_{k\le n} \Delta t^k$. To obtain second-order accuracy in time, the two-stage second-order TVD Runge-Kutta scheme is adopted. At the kth stage, $k \in \{1,2\}$, the two-step projection-correction method is given by:

$$\begin{aligned} \frac{\mathbf{U}^{(\tilde{k})} - \mathbf{U}^{(k-1)}}{\Delta t} + \partial_x \mathbf{F}(\mathbf{U}^{(k-1)}) + \mathbf{B}(\mathbf{U}^{(k-1)})\partial_x \mathbf{U}^{(k-1)} + \mathbf{G}(\mathbf{U}^{(k-1)})\partial_x z_b &= 0, \\ \frac{\mathbf{U}^{(k)} - \mathbf{U}^{(\tilde{k})}}{\Delta t} - \mathcal{T}(h^{(k)}, \partial_x h^{(k)}, z_b, \partial_x z_b, \mathbf{P}^{(k)}, \partial_x \mathbf{P}^{(k)}) &= 0 \\ \mathcal{B}(\mathbf{U}^{(k)}, \partial_x \mathbf{U}^{(k)}, z_b, \partial_x z_b) &= 0 \end{aligned} \tag{S8}$$

where $U^{(0)}$ is U at the time level t^n, $U^{(\tilde{k})}$ is an intermediate value in the two-step projection-correction method that contains the numerical solution of the hyperbolic system (S1) at the corresponding kth stage of the Runge-Kutta, and $U^{(k)}$ is the $k-th$ stage estimate. After that, a final value of the solution at the t^{n+1} time level is obtained:

$$\mathbf{U}^{n+1} = \frac{1}{2}\mathbf{U}^n + \frac{1}{2}\mathbf{U}^{(2)}. \tag{S9}$$

Observe that equations

(S8) require, at each stage of the calculation respectively, to solve a Poisson-like equation for each one of the variables contained in $P^{(k)}$. The resulting linear system is solved using an iterative Jacobi method combined with a scheduled relaxation (see Adsuara et al., 2016; Escalante et al., 2018, 2019). Note that the usual CFL restriction must be imposed for the computation of the time step Δt.

When friction with the bottom (τ_α^u), viscous shear stress $\left(K_{\alpha+1/2}\right)$, and the breaking model (τ_α^w) are considered, they will be computed semi-implicitly at the end of the second step of the projection-correction method at each kth stage of the TVD Runge-Kutta method as it is done in (Escalante et al., 2019). Note that the resolution of a straightforward tridiagonal system on the vertical for each volume I_i is exclusively required for the viscosity model. In contrast, the friction and breaking models can be considered by solving conventional algebraic problems, as is commonly the practice for friction models.

The resulting numerical scheme is well-balanced for the water at rest solution and is linearly L^∞-stable under the usual CFL condition related to the hydrostatic system. It is also worth mentioning that the numerical scheme is positive preserving and can deal with emerging topographies.

Text S2 Benchmark comparison

S2.1 Propagation of regular non-breaking waves over submerged bar

The experiments discussed in references (Beji & Battjes, 1994; Dingemans, 1994) conducted in a wave flume featuring a submerged trapezoidal bar, are well-known as a significant benchmark for dispersive models. In this test case, the spatial domain spans from 0 to 30 meters and includes a submerged trapezoidal obstacle, as depicted in Figure S3. The domain is discretized into cells with a constant length of Δx = 0.02 meters. An incident sinusoidal wave train is applied as a boundary condition on the left-hand side of the domain at x = 0 meters, following the approach described in (Escalante et al., 2019) with the following parameters:

$$\eta_l(t) = A \sin\left(\frac{2\pi}{T} t\right) \tag{S10}$$

where $A = 0.01$ meters and $T = 2.02$ seconds represent the amplitude and period, respectively. The remaining flow variables at $x = 0$ meters are set to zero. On the right side of the domain, free-outflow boundary conditions are enforced. The friction term is set to $n = 0.01$ in this test, and the CFL number is set to 0.9.

The resulting wave train is measured at eight wave gauge stations denoted as *WG1*, *WG2*, . . . ,*WG8* for the free-surface elevation η (see Figure S3). Figure S4 compares numerical simulations and experimental laboratory observations at various gauge points. Initially, we observe a good agreement for the two-layer model ($L = 2$) with the experimental data, and there is a slight improvement in results when the number of layers is increased to $L = 3$.

It's worth noting that we corroborate similar observations found in the literature, such as that in Ma et al. (2012) which utilizes σ-coordinates, or Escalante et al., (2019), where an enhanced two-layer version of the nonhydrostatic pressure multilayer system described here is employed. The findings in Chazel et al. (2011) with a three-parameter Green-Naghdi model optimized for uneven bottoms exhibit a comparable level of agreement.

S2.2 Solitary wave runup impinging on a plane beach

A classic test for dispersive shallow flows corresponds to the experimental setup by (Titov & Synolakis, 1995). Incident solitary waves of multiple relative amplitudes A/H^* were simulated to study propagation, breaking, and runup over a planar beach with a slope of 1:19.85 (corresponding to a bathymetry angle of about 2.9°). Experimental data are available in (Titov & Synolakis, 1995) for surface elevation at different times.

We consider the bathymetry of the problem as described in Figure 5. The computational domain [−15, 70] m is covered with cells of constant length $\Delta x = 0.01\, m$. The CFL number is set to 0.9, and free-outflow boundary conditions were imposed everywhere.

We begin by considering the initial condition for the model provided by a solitary wave of amplitude $A = 0.3m$ centered at point $x = 25m$ (see Escalante et al., 2018) for details on the expression of the solitary wave). In this case, a friction coefficient of n = 0.02 was used to account for the glass surface roughness effects appearing in the experiments. Figure S6 shows snapshots at different times, $t\sqrt{g/H^*} = t_0$. A good agreement between experimental and simulated

data is seen. We remark that wave breaking is observed at $t\sqrt{g/H^*} = 20$ and 25 during the experiment. The breaking criteria mechanism is mandatory, as it can be seen in Figure S7 where, independently of the number of layers, a nonphysical overshoot on the flow variables arise when waves start to break without any breaking dissipation mechanism as the one considered here.

Then, we consider the numerical simulation of solitary waves of different wave amplitudes $A = 0.1, A = 0.2, \ldots, A = 0.6\,m$, and compute the maximum runup for each test case, and for different values of the Manning parameter $n = 0.013, n = 0.015, n = 0.02$ and $n = 0.025$, and number of layers $L = 1, L = 3$. Furthermore, the numerical tests were run considering hydrostatic and non-hydrostatic pressure.

We then plot and compare the results with the experimental results given in (Titov & Synolakis, 1995) (See Figure S8). We first observe consistency on the computed numerically runup when considering different numbers of layers and hydrostatic or non-hydrostatic regimes. Moreover, we perform a sensitivity numerical analysis by considering a reasonable range for the Manning coefficient and observe good consistency in the runup results.

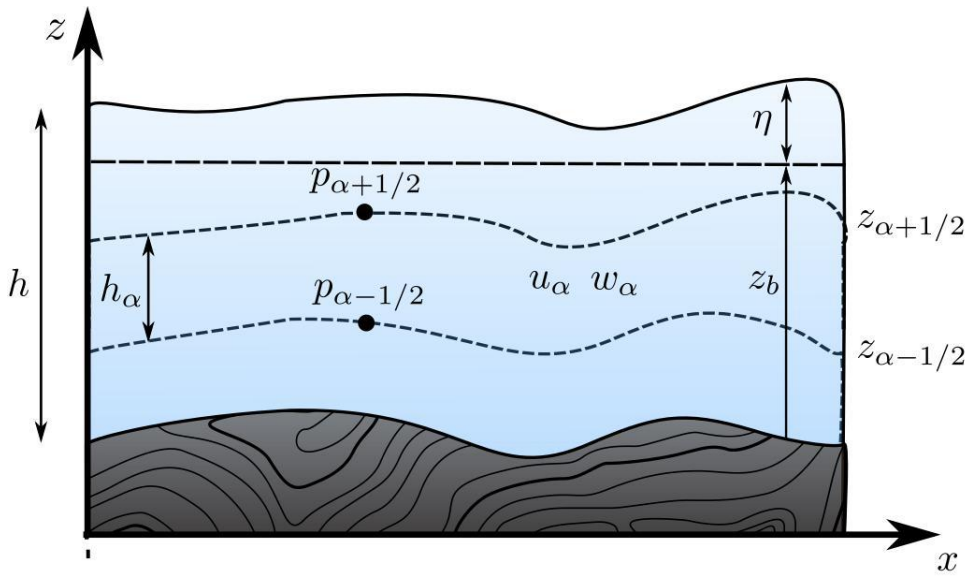

Figure S1. Schematic diagram describing the multilayer system

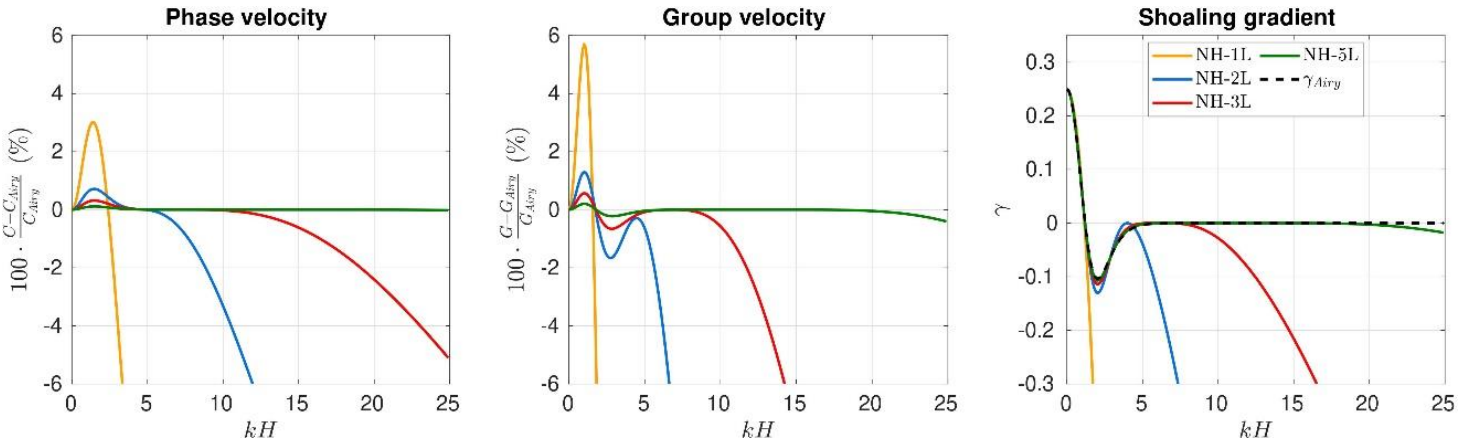

Figure S2. Relative error for the phase velocities (left), the group velocities (center), and comparison with the reference shoaling gradient (right), w.r.t. the Airy theory for NH-ML systems. NH-$\boldsymbol{x}$L stands for NH-ML system with L = 1, 2, 3, 5 layers.

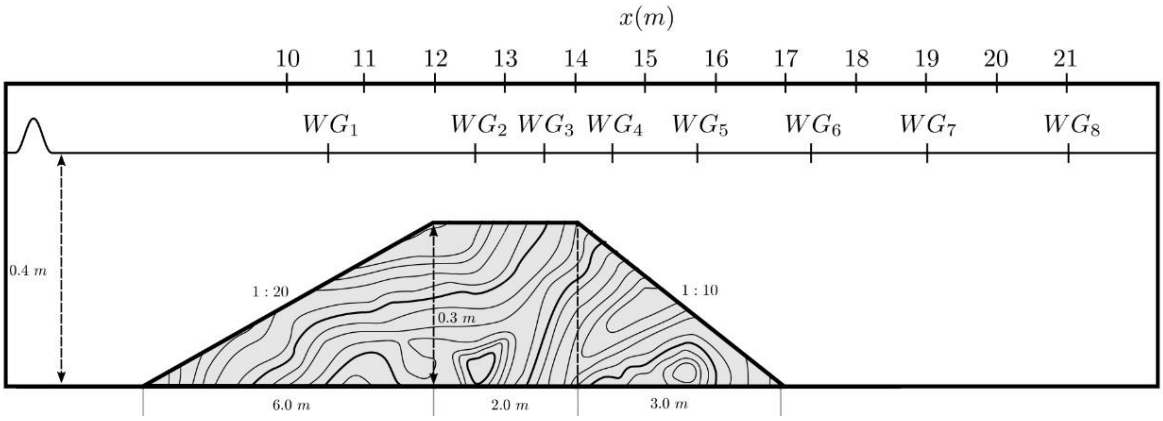

Figure S3. Periodic waves breaking over a submerged bar. Sketch of the topography and layout of the wave gauges

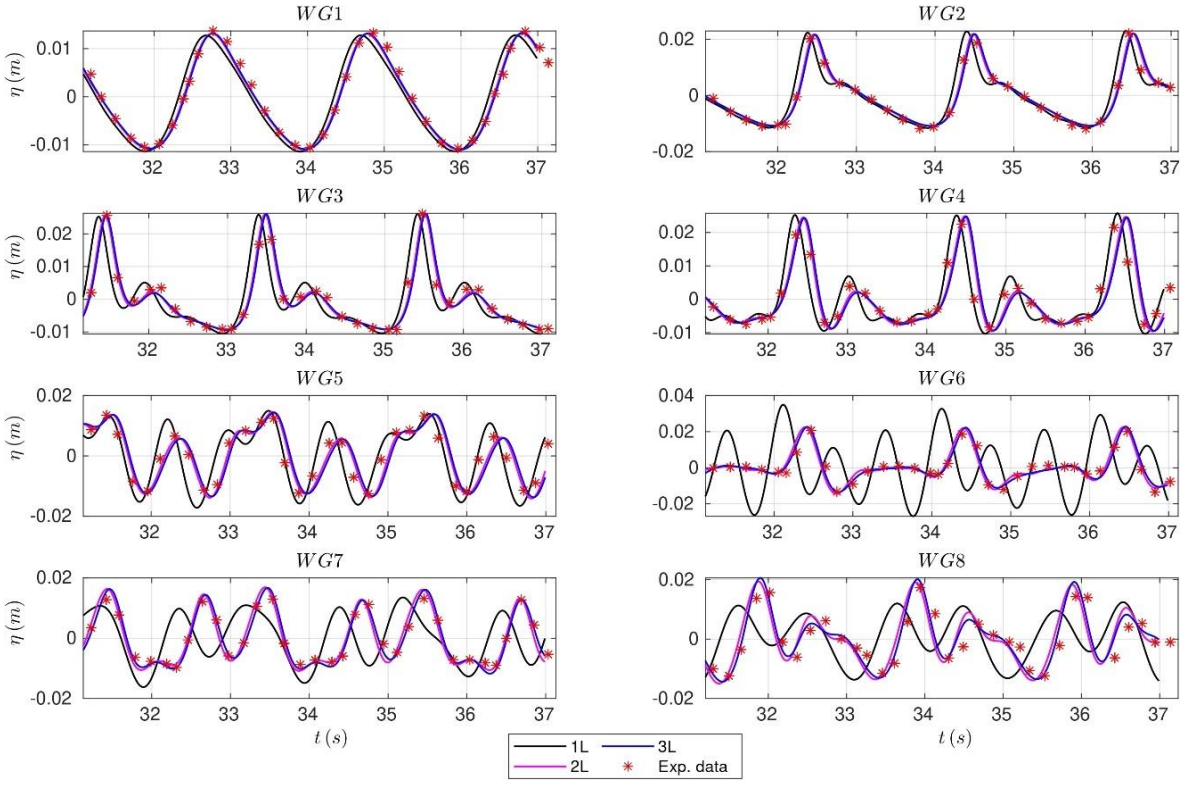

Figure S4. Comparison of data time series (red star points) and numerical values at wave gauges *WG1*, *WG2*, *WG3*, *WG4*, *WG5*, *WG6*, *WG7*, *WG8*.

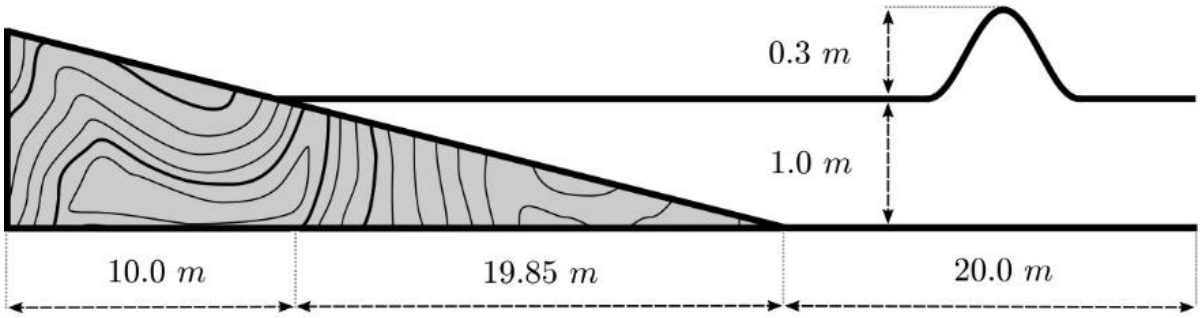

Figure S5. Sketch of the topography mimicking a beach

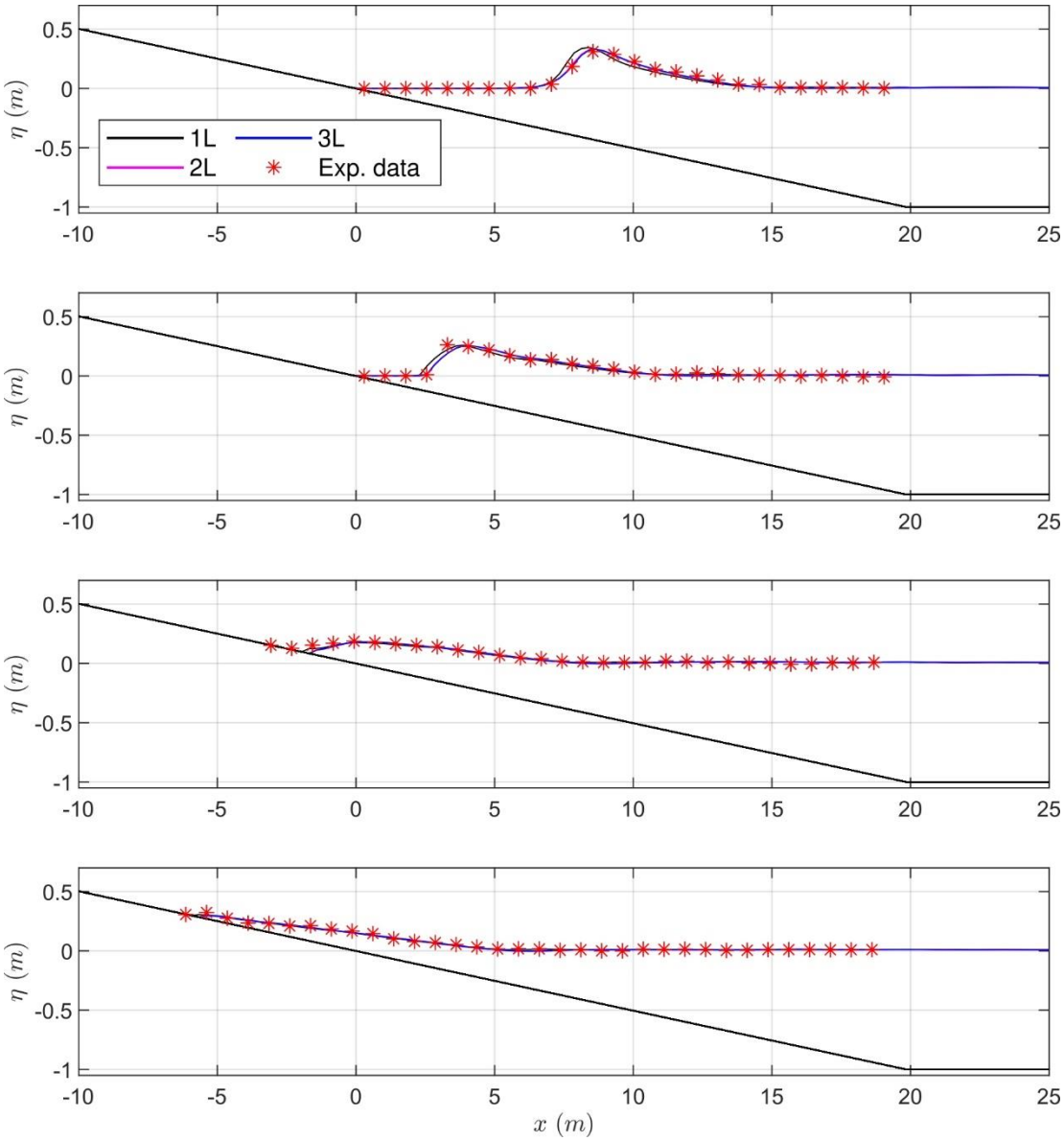

Figure S6. Comparison of experimental data (star points) and simulated ones (solid lines) at times $t\sqrt{g/H} = 15, 20, 25, 30$.

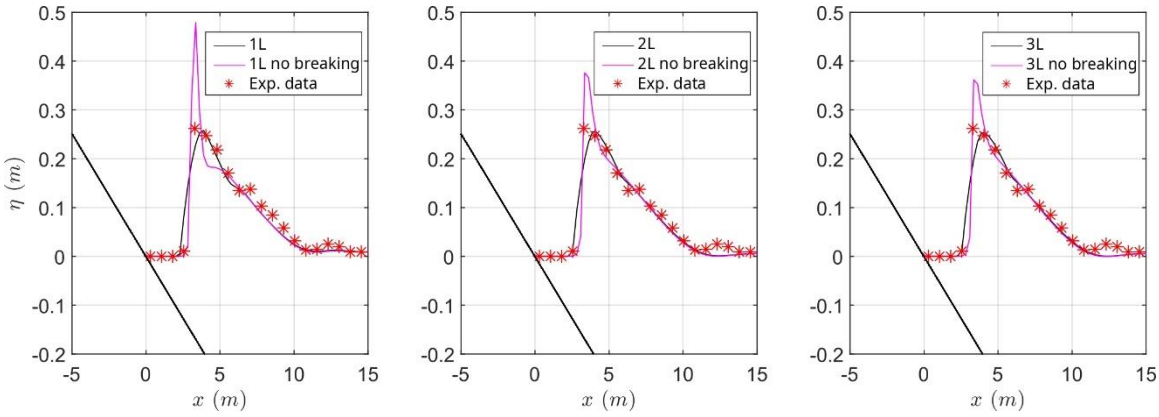

Figure S7. Comparison of experimental data (star points) and simulated ones (solid lines) at time $t\sqrt{g/H} = 20$

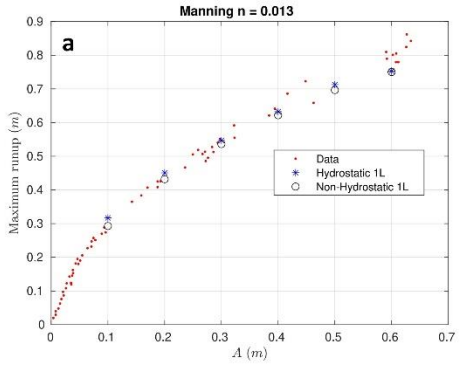
Manning n = 0.013
a
Data
Hydrostatic 1L
Non-Hydrostatic 1L
Maximum runup (m)
A (m)

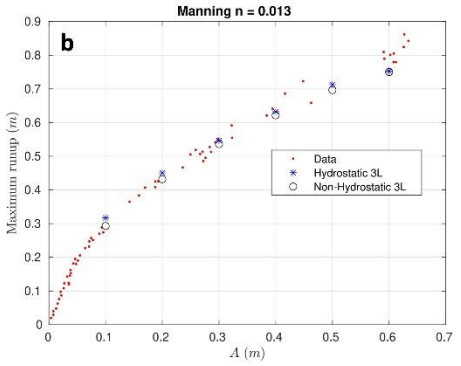
Manning n = 0.013
b
Data
Hydrostatic 3L
Non-Hydrostatic 3L
Maximum runup (m)
A (m)

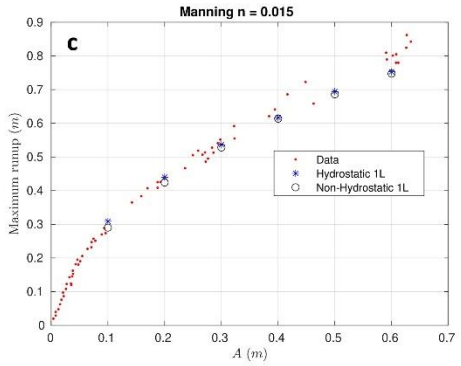
Manning n = 0.015
c
Data
Hydrostatic 1L
Non-Hydrostatic 1L
Maximum runup (m)
A (m)

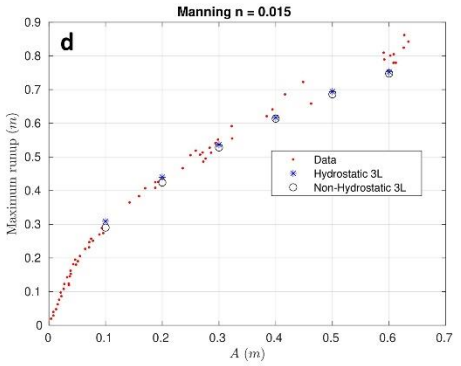
Manning n = 0.015
d
Data
Hydrostatic 3L
Non-Hydrostatic 3L
Maximum runup (m)
A (m)

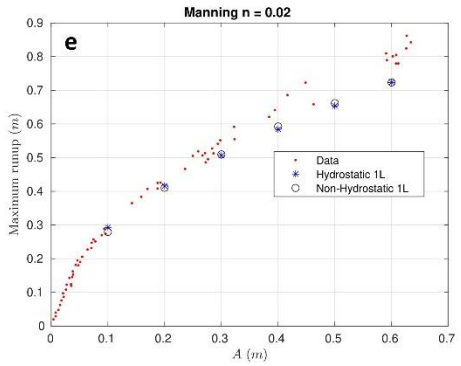
Manning n = 0.02
e
Data
Hydrostatic 1L
Non-Hydrostatic 1L
Maximum runup (m)
A (m)

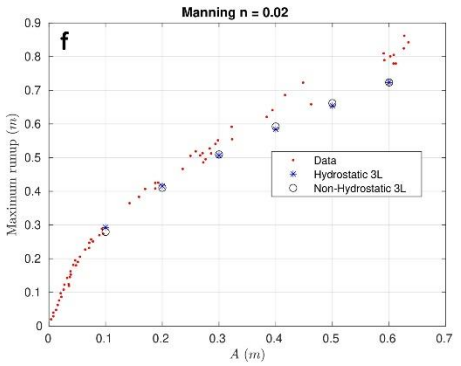
Manning n = 0.02
f
Data
Hydrostatic 3L
Non-Hydrostatic 3L
Maximum runup (m)
A (m)

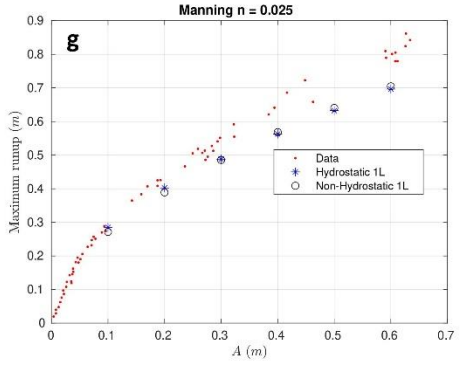
Manning n = 0.025
g
Data
Hydrostatic 1L
Non-Hydrostatic 1L
Maximum runup (m)
A (m)

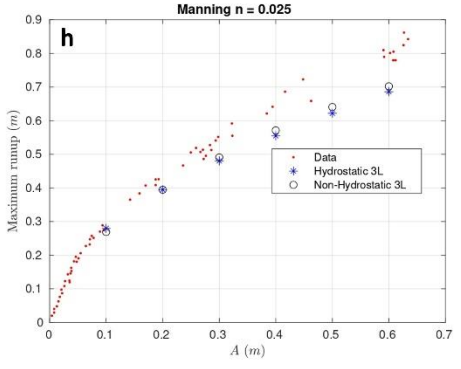
Manning n = 0.025
h
Data
Hydrostatic 3L
Non-Hydrostatic 3L
Maximum runup (m)
A (m)

Figure S8. Experimental maximum runup (red points) and numerically computed maximum runups. A sensitivity numerical study considering different numbers of layers (1L a-c-e-g, 3L b-d-f-h), Manning coefficient n (0.013, 0.015, 0.02 and 0.025 for panels a-b, c-d, e-f, g-h respectively), and pressure regimes (Hydrostatic Non-Hydrostatic).

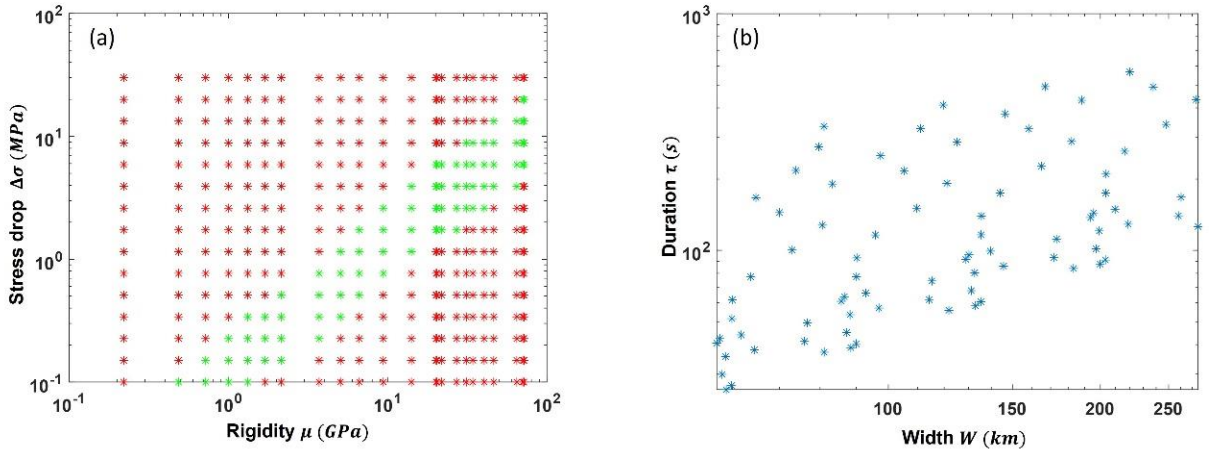

Figure S9. Parameters of the set of the simulated sources. (a) Stress drop and rigidity for all the possible combination of parameters in Table S1. Green stars represent the 81 selected simulations (See Table S2) while the red stars indicate the discarded ones according to the parametric choices described in Section 3. (b) The 81 selected simulations are plotted accordingly to their duration τ and width W.

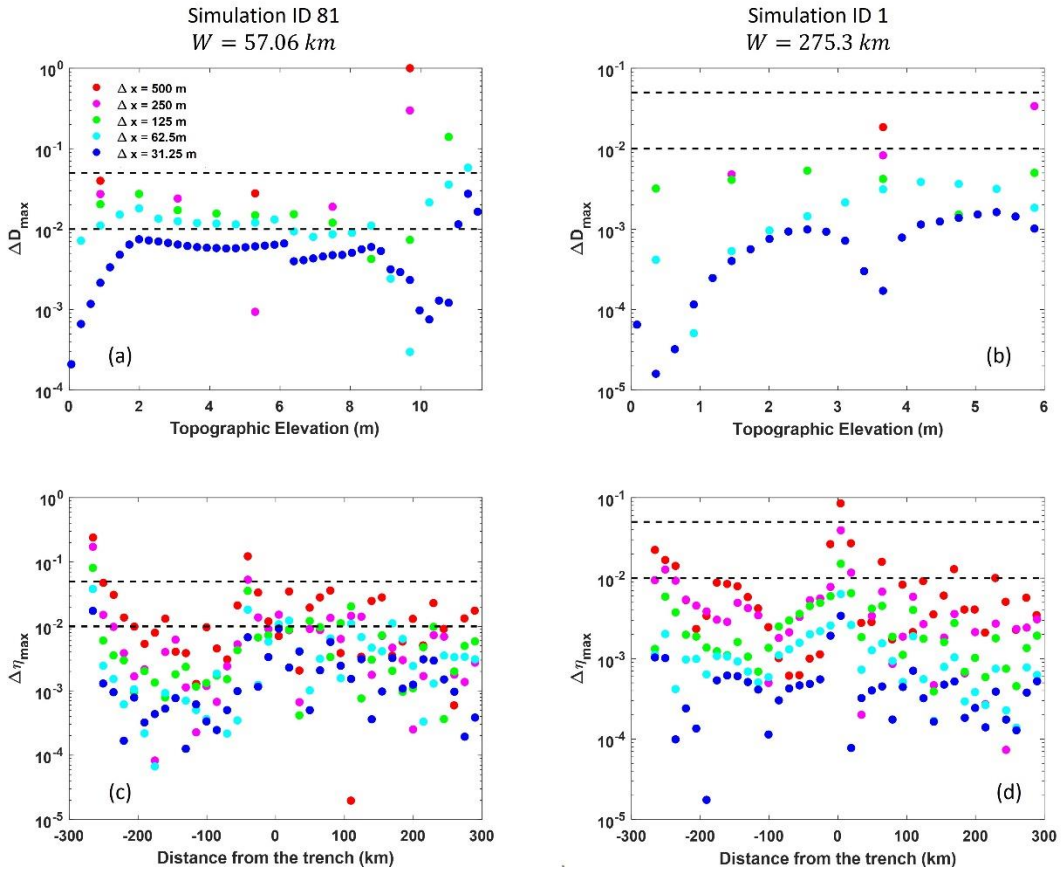

Figure S10. Results of convergence tests. (a) and (b): ΔD_{max} computed with respect to the reference grid ($\Delta x = 15.625\ m$) at different topographic elevation up to the maximum run-up for simulation ID 81 and 1 respectively. Different colors refer to different grids as indicated in the legend within the panel (a). The black dashed lines represent $\Delta D_{max} = 0.01$ and $\Delta D_{max} = 0.05$ levels. (c) and (d): $\Delta \eta_{max}$ computed with respect to the reference grid ($\Delta x = 15.625\ m$) at different distances from the trench both rightward and leftward (towards to the coast) from the source, for simulation ID 81 and 1 respectively. Different colors refer to different grids as indicated in the legend within the panel (a). The black dashed lines represent $\Delta \eta_{max} = 0.01$ and $\Delta \eta_{max} = 0.05$ levels.

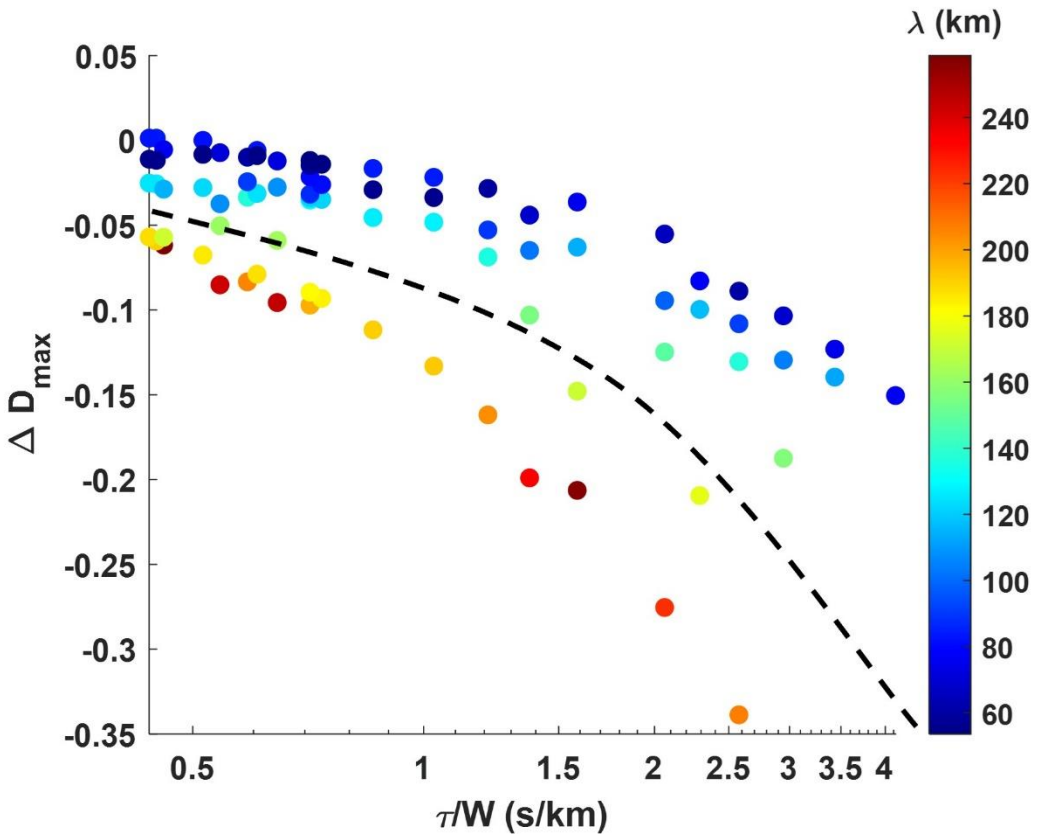

Figure S11. Relative discrepancy ΔD_{max} between time-dependent shallow water (TD-SW) and instantaneous source shallow water (IS-SW) results in terms of flow-depth at the first point on the coast as a function of τ/W with color scale marking the source horizontal extension λ. The black dashed line separates the two highlighted trends for small and large ruptures similarly to what is shown in the Figure 4(a) for the non-hydrostatic case.

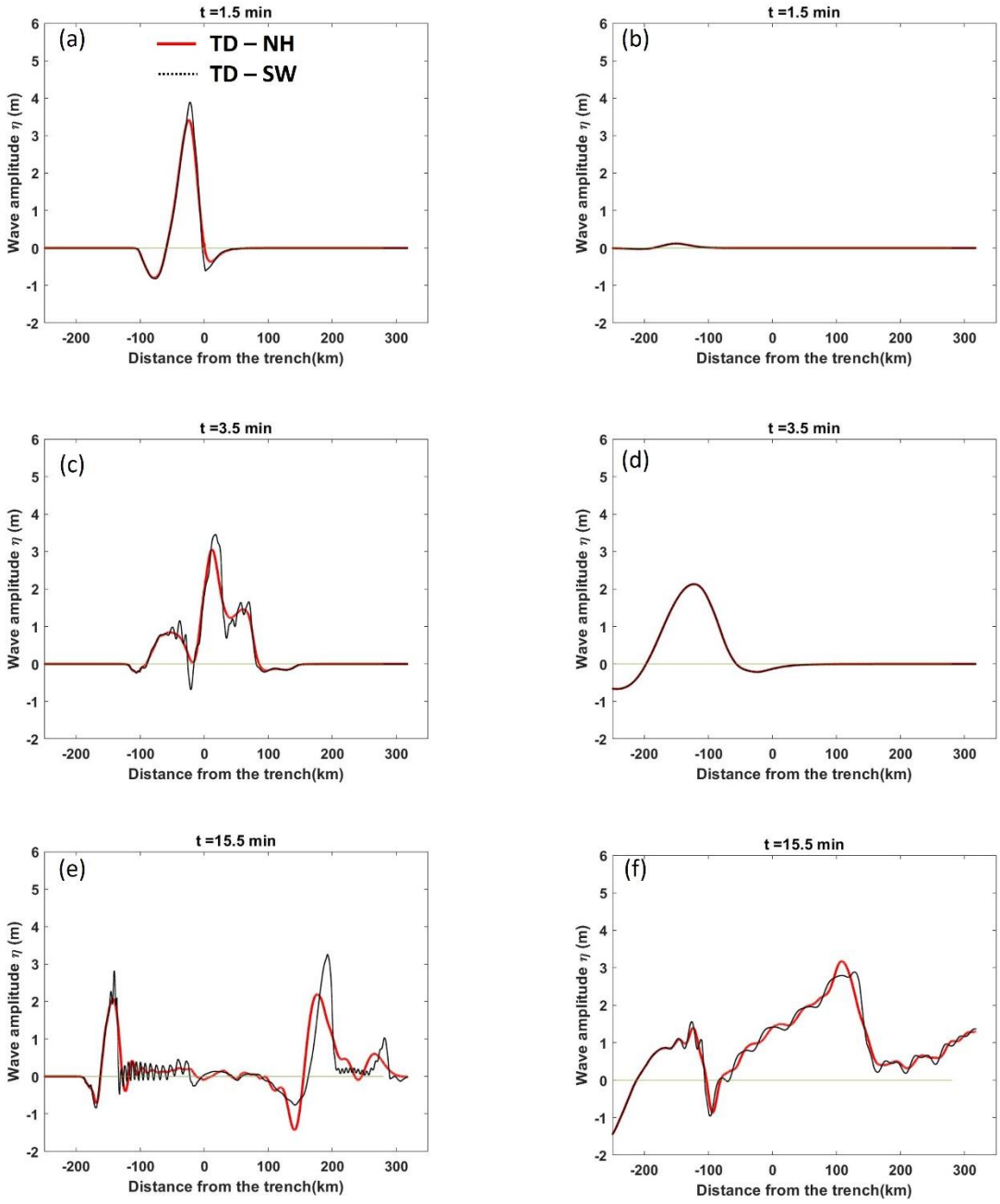

Figure S12. Wave amplitude as a function of the distance from the trench for TD – NH (red curves) and TD – SW (black dotted lines) at three different time steps and for two simulations: the ID 70 (left panels) and the ID 7 (right panels) in Table S2. These simulations

represent examples of small and large size sources respectively. The whole evolution can be found in the Supporting Information (Movie S5 and S6)

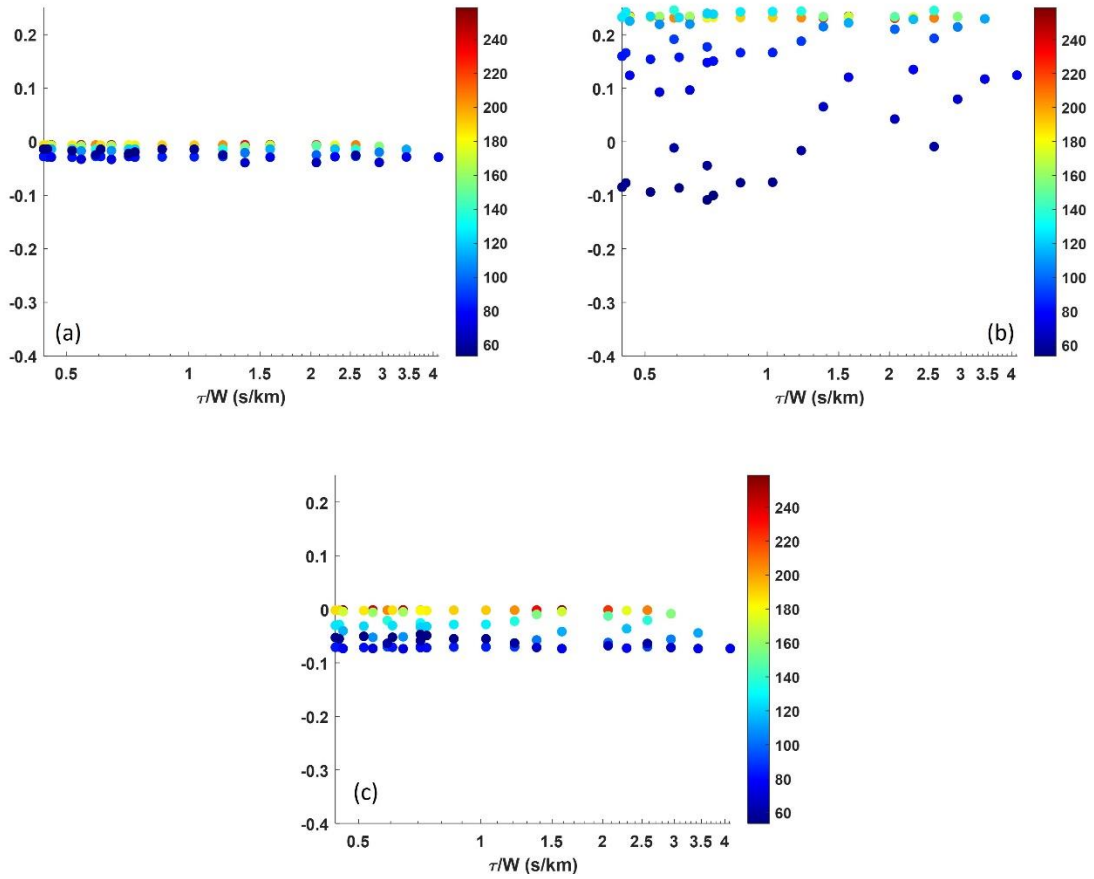

Figure S13. Relative discrepancy between Non-Hydrostatic (NH) and Shallow Water (SW) results when IS sources are used for both propagation regime. (a) $\Delta\eta_{max}$ at a gauge placed along the coastward propagation as a function of τ/W with color scale marking the source horizontal extension λ. (b) $\Delta\eta_{max}$ at a gauge placed rightward beyond the trench as a function of τ/W with color scale marking the source horizontal extension λ. (c) ΔD_{max} at the first point on coast as a function of τ/W with color scale marking the source horizontal extension λ. For sake of comparison the figures are plotted with the same scale.

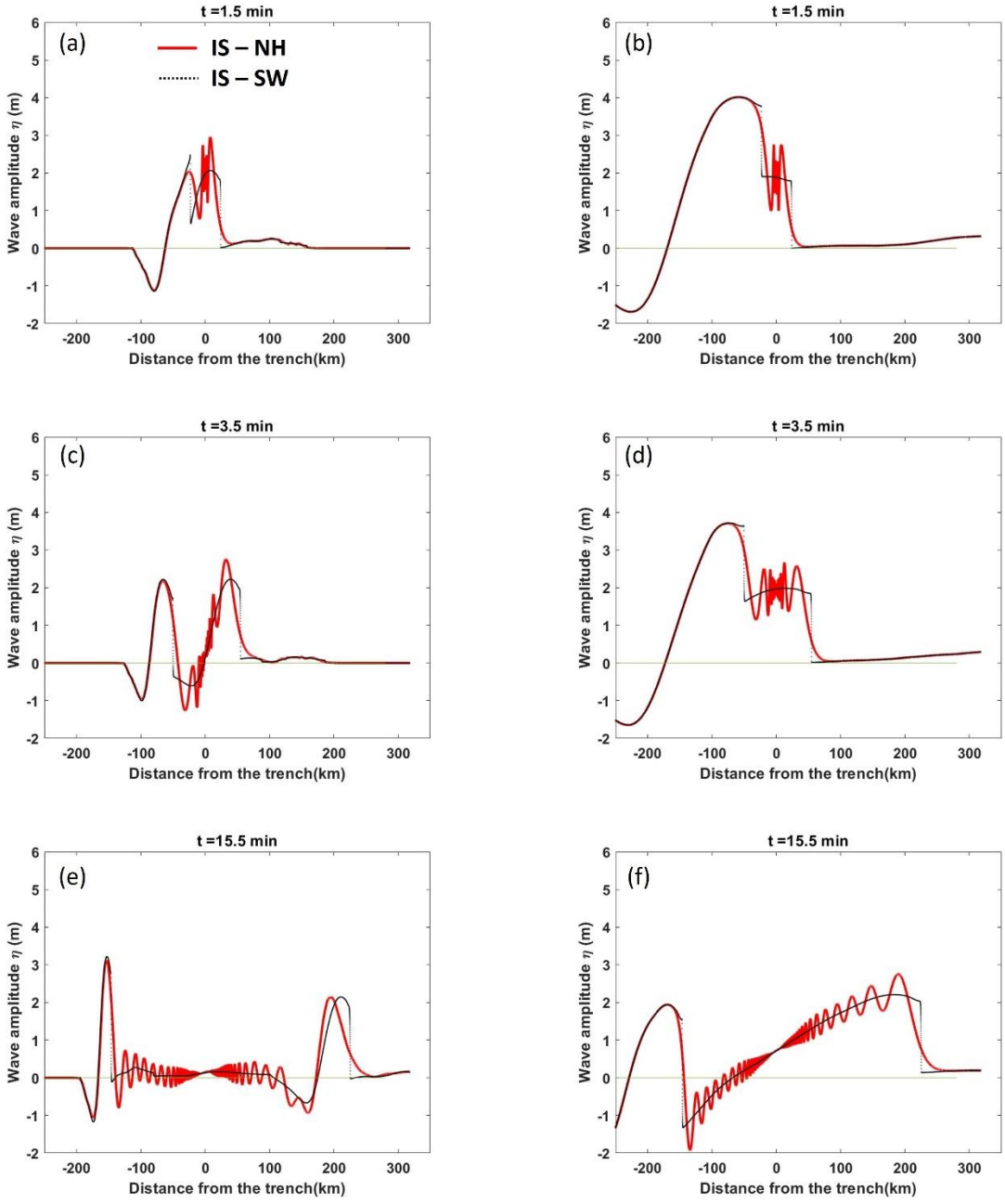

Figure S14. Wave amplitude as a function of the distance from the trench for IS – NH (red curves) and IS – SW (black dotted lines) at three different time steps and for two simulations: the ID 70 (left panels) and the ID 7 (right panels) in Table S2. These simulations

represent examples of small and large size sources respectively. The whole evolution can be found in the Supporting Information (Movie S7 and S8)

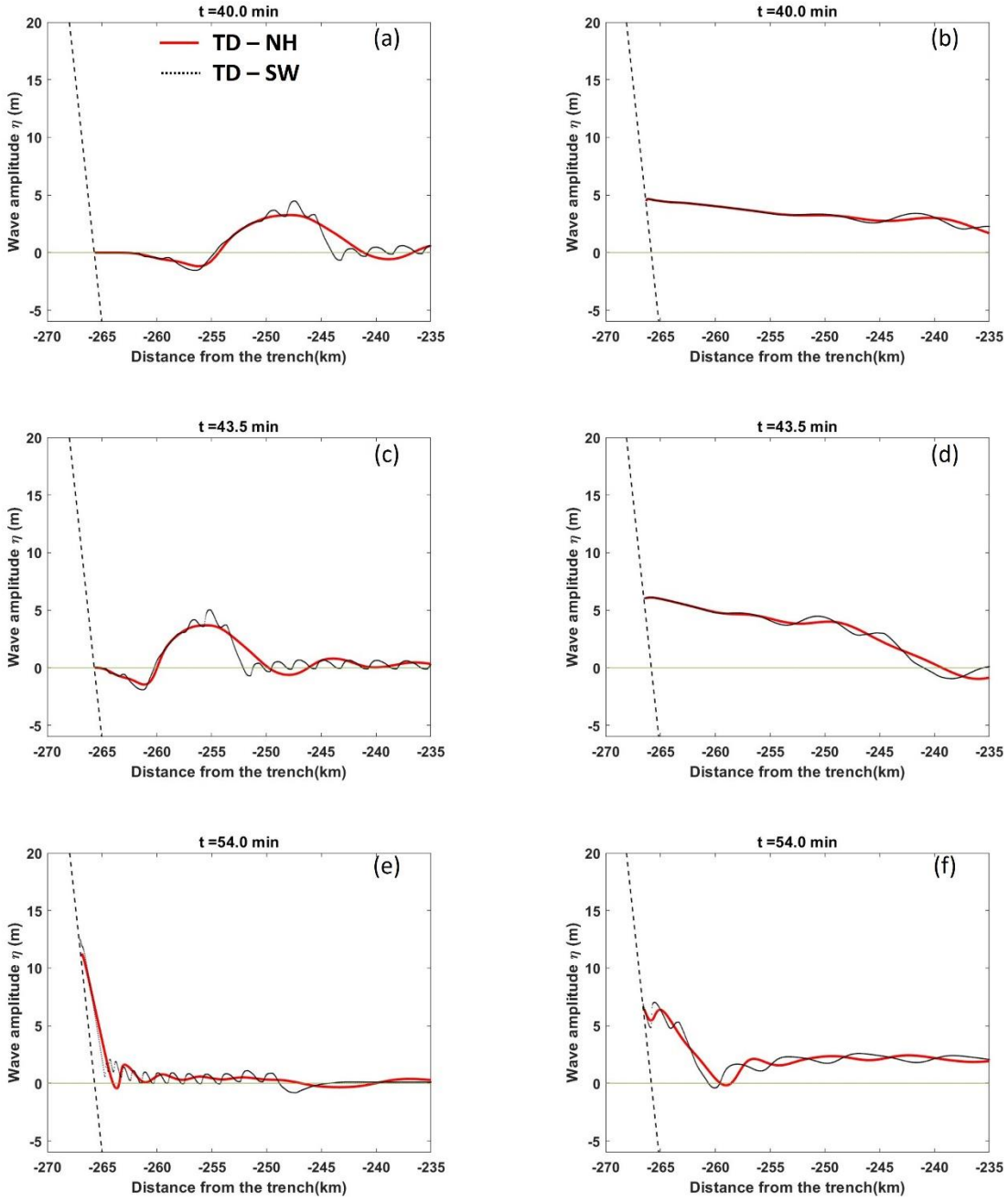

Figure S15 Wave amplitudes, zoomed around the coast, as a function of the distance from the trench for TD – NH (red curves) and TD – SW (black dotted lines) at three different time steps and for two simulations: the ID 70 (left panels) and the ID 7 (right panels) in Table S2. These simulations represent examples of small and large size sources respectively. The

short-dashed line on the left represents the coast line within each panel. The whole evolution can be found in the Supporting Information (Movie S9 and S10).

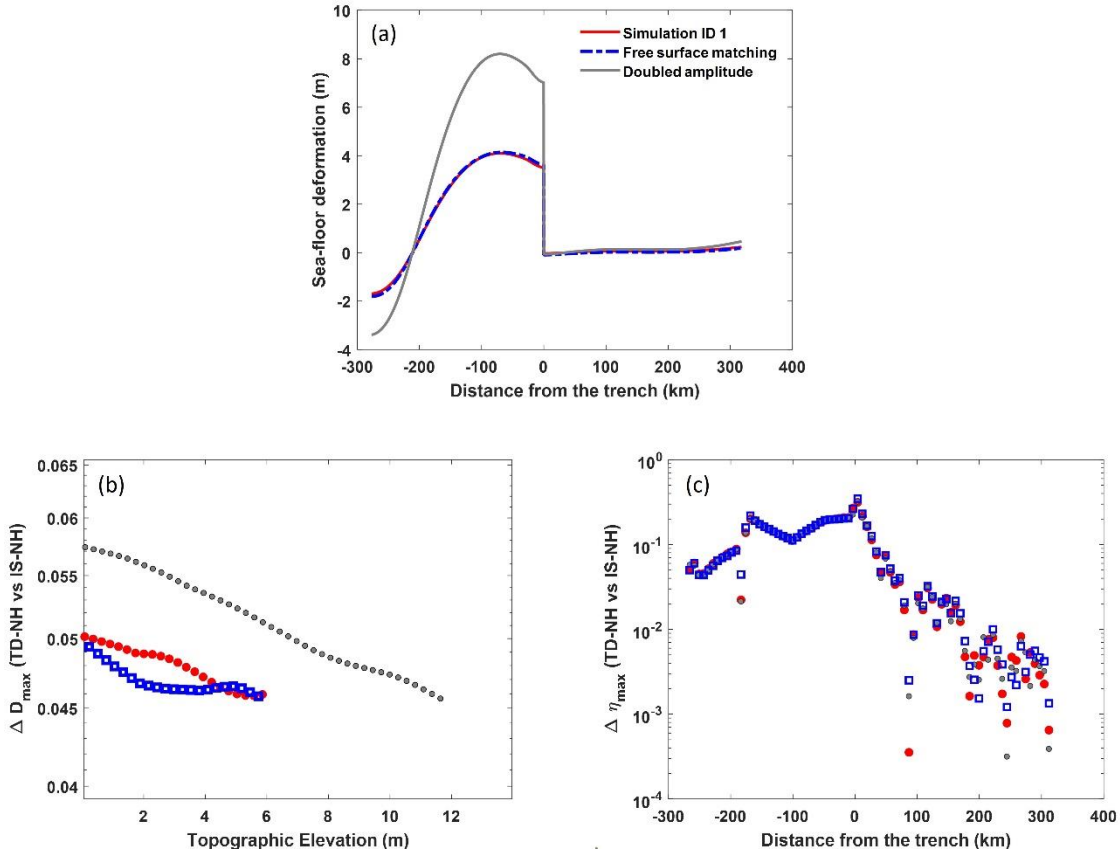

Figure S16 (a): Final sea-floor deformation for the simulation ID 1 in Table S2 (on the "Tohoku Hypo" bathymetry, red curve, "Simulation ID 1" in the legend) compared to the sea-floor deformation generated by a rupture dynamic simulation performed with a perfect matching between the free surface and the tsunami simulation bathymetry (blue dashed curve, "Free surface matching" in the legend). The grey curve represents a final sea-floor deformation with a doubled amplitude as compared to the red curve (grey curve, "Doubled amplitude" in the legend). For this test, these deformations have been used as initial conditions for further TD-NH (simulated with the same source dynamics) and IS-NH simulations. (b) ΔD_{max} (TD-NH vs IS-NH) at different topographic elevations for the initial conditions described in panel (a) (with the same color scheme). "Simulation ID 1" and "Free surface matching" simulations lead to ΔD_{max} values in the same range ([4.6%-5.0%]) converging to the same value in the vicinity of the maximum run-up. As expected, the high amount of available energy for "Doubled amplitude" simulations lead to larger discrepancies between IS and TD sources at the first points on the coast. Nevertheless, in the vicinity of the maximum run-up (doubled as compared to the other simulations) the ΔD_{max} converges to a consistent value as compared to the one from "Simulation ID 1". (c) $\Delta\eta_{max}$ (TD-NH vs IS-NH) offshore as a function of distance from the trench for the initial

conditions described in panel (a) (with the same color scheme). Regardless of the different initial conditions $\Delta\eta_{max}$ takes on consistent values.

Table S1. Elastic and rheological parameters used to re-scale the dimensionless outputs of rupture dynamic simulations. In the last it is reported the subduction layer that can be realistically associated to the correspondent V_s, ρ and μ values

#	$\boldsymbol{V_s}$ $(\boldsymbol{km/s})$	$\boldsymbol{\rho}$ $(\boldsymbol{g/cm^3})$	$\boldsymbol{\mu}$ $(\boldsymbol{GPa})$	***Layer***
1	0,35	1,80	0,22	Accretionary prism
2	0,5	1,95	0,49	//
3	0,6	2,00	0,72	//
4	0,7	2,05	1,00	//
5	0,8	2,07	1,32	//
6	0,9	2,10	1,70	//
7	1,0	2,15	2,15	//
8	1,3	2,20	3,72	//
9	1,5	2,25	5,06	//
10	1,7	2,30	6,65	//
11	2,0	2,35	9,4	//
12	2,4	2,45	14,11	//
13	2,9	2,60	21,87	Seismic bedrock
14	3,2	2,65	27,14	//
15	3,4	2,70	31,21	Upper crust layer
16	3,8	2,80	40,43	Lower crust
17	4,5	3,20	64,80	Mantle
18	2,8	2,60	20,38	Oceanic layer 1
19	2,9	2,40	20,18	//
20	3,5	2,80	34,3	Oceanic layer 2
21	4,0	2,90	46,4	//
22	4,6	3,40	71,94	Oc.-Cont. Mantle
23	4,7	3,20	70,69	Oceanic Mantle

Table S2 (In a separate file) Parameters (S-wave velocity, rigidity, stress drop and Dc from column to 2 to 5), duration (column 6) and width (column 7) for the 81 selected source models. They are ordered as indicated in column 1.

Table S3 Real subduction events used in Figure 8, classified according to their Moment magnitude Mw, stress drop, duration, width and dip

Event	**Date**	**Mw**	**Stress Drop (MPa)**	**Duration (s)**	**Width (km)**	**Dip (°)**
Nicaragua	1992-09-02	7.62	0.78	100	70	15
Java-Bali	1994-06-02	7.75	0.65	64	120	12
Peru	1996-02-21	7.50	0.76	79	70	14
Sumatra 2004	2004-12-26	9.10	4.3	567.35	330	16
Nias-Simeuleu	2005-03-28	8.61	1.20	142	275	8
Java-Pangandaran	2006-06-17	7.71	1.66	144.5	70	10
Sumatra 2007	2007-09-12	8.48	3.19	109	180	12
Papua	2009-01-03	7.66	1.75	51	65	28
Maule	2010-02-27	8.78	3.16	122	180	18
Tohoku foreshock	2011-03-09	7.34	1.76	22.5	55	12
Tohoku	2011-03-11	9.08	12.50	157.5	220	10
Iquique	2014-04-01	8.08	7.66	77.5	90	18

Movie S1. Wave amplitude time-evolution as a function of the distance from the trench for the simulations shown in Figures 2(a), 2(c) and 2(e).

Movie S2. Wave amplitude time-evolution as a function of the distance from the trench for the simulations shown in Figures 2(b), 2(d) and 2(f).

Movie S3. Inundation time-evolution as a function of the distance from the trench for the simulations shown in Figures 3(a), 3(c) and 3(e).

Movie S4. Inundation time-evolution as a function of the distance from the trench for the simulations shown in Figures 3(b), 3(d) and 3(f).

Movie S5. Wave amplitude time-evolution as a function of the distance from the trench for the simulations shown in Figures S12(a), S12(c) and S12(e) in Supporting Information.

Movie S6. Wave amplitude time-evolution as a function of the distance from the trench for the simulations shown in Figures S12(b), S12(d) and S12(f) in Supporting Information.

Movie S7. Wave amplitude time-evolution as a function of the distance from the trench for the simulations shown in Figures S14(a), S14(c) and S14(e) in Supporting Information.

Movie S8. Wave amplitude time-evolution as a function of the distance from the trench for the simulations shown in Figures S14(b), S14(d) and S14(f) in Supporting Information.

Movie S9. Inundation time-evolution as a function of the distance from the trench for the simulations shown in Figures S15(a), S15(c) and S15(e) in Supporting Information.

Movie S10. Inundation time-evolution as a function of the distance from the trench for the simulations shown in Figures S15(b), S15(d) and S15(f) in Supporting Information.

References

Adsuara, J. E., Cordero-Carrión, I., Cerdá-Durán, P., & Aloy, M. A. (2016). Scheduled Relaxation Jacobi method: Improvements and applications. *Journal of Computational Physics*, *321*, 369–413. https://doi.org/10.1016/j.jcp.2016.05.053

Beji, S., & Battjes, J. A. (1994). Numerical simulation of nonlinear wave propagation over a bar. *Coastal Engineering*, *23*(1–2), 1–16. https://doi.org/10.1016/0378-3839(94)90012-4

Castro Díaz, M. J., & Fernández-Nieto, E. (2012). A Class of Computationally Fast First Order Finite Volume Solvers: PVM Methods. *SIAM Journal on Scientific Computing*, *34*(4), A2173–A2196. https://doi.org/10.1137/100795280

Chazel, F., Lannes, D., & Marche, F. (2011). Numerical Simulation of Strongly Nonlinear and Dispersive Waves Using a Green–Naghdi Model. *Journal of Scientific Computing*, *48*(1–3), 105–116. https://doi.org/10.1007/s10915-010-9395-9

Chorin, A. J. (1968). Numerical Solution of the Navier-Stokes Equations. *Mathematics of Computation*, *22*(104), 745. https://doi.org/10.2307/2004575

Dingemans, M. W. (1994). *MAST PROJECT 1: WAVES G8-M Comparison of computations with Boussinesq-like models and laboratory measurements*.

Escalante, C., Fernández-Nieto, E. D., Morales de Luna, T., & Castro, M. J. (2019). An Efficient Two-Layer Non-hydrostatic Approach for Dispersive Water Waves. *Journal of Scientific Computing*, *79*(1), 273–320. https://doi.org/10.1007/s10915-018-0849-9

Escalante, C., Morales de Luna, T., & Castro, M. J. (2018). Non-hydrostatic pressure shallow flows: GPU implementation using finite volume and finite difference scheme. *Applied Mathematics and Computation*, *338*, 631–659. https://doi.org/10.1016/j.amc.2018.06.035

Kazolea, M., & Delis, A. I. (2013). A well-balanced shock-capturing hybrid finite volume–finite difference numerical scheme for extended 1D Boussinesq models. *Applied Numerical Mathematics*, *67*, 167–186. https://doi.org/10.1016/j.apnum.2011.07.003

Ma, G., Shi, F., & Kirby, J. T. (2012). Shock-capturing non-hydrostatic model for fully dispersive surface wave processes. *Ocean Modelling*, *43–44*, 22–35. https://doi.org/10.1016/j.ocemod.2011.12.002

Ricchiuto, M., & Filippini, A. G. (2014). Upwind residual discretization of enhanced Boussinesq equations for wave propagation over complex bathymetries. *Journal of Computational Physics*, *271*, 306–341. https://doi.org/10.1016/j.jcp.2013.12.048

Titov, V. V., & Synolakis, C. E. (1995). Modeling of Breaking and Nonbreaking Long-Wave Evolution and Runup Using VTCS-2. *Journal of Waterway, Port, Coastal, and Ocean Engineering*, *121*(6), 308–316. https://doi.org/10.1061/(ASCE)0733-950X(1995)121:6(308)